Diffusion and thermodiffusion studies in ferrofluids with a new two-dimensional forced Rayleigh-scattering technique

G Demouchy[1], A Mezulis[1], A Bee[2], D Talbot[2], J C Bacri[1] and A Bourdon[1]

[1] Laboratoire des Milieux Désordonnés et Hétérogènes, UMR 7603 du CNRS, Campus Boucicaut, Université Pierre et Marie Curie, 140 rue de Lourmel, 75015 Paris, France
[2] LI2C Colloïdes inorganiques, UMR 7612 du CNRS, Université Pierre et Marie Curie, case 63, 4 place Jussieu, 75252 Paris Cedex 05, France

Abstract
In this paper, we present a new simple two-dimensional forced Rayleigh-scattering (FRS) experimental set-up for determination of the nanoparticle-diffusion coefficient (D_M) and the Soret coefficient (S_T) in colloids. For this purpose, we give a two-timescale model for the evolutions of temperature and colloid concentration (similar to that given for a former one-dimensional FRS method) and a complete description of the signals diffracted by a squared-lattice grating. Both transport properties in ferrofluids (magnetic colloids) determined with this new set-up are in good agreement with those found with samples already studied using the one-dimensional technique. This work is completed by studying new samples. Experimental results we obtained confirm and make clearer the following: (i) the strong Soret effect in ferrofluids has a nanoparticle origin and (ii) furthermore, this origin lies in the immediate surroundings of the nanoparticles (ionic or surfaced coating and dispersion liquid).

1. Introduction

Thermodiffusion (also called the Soret effect or Ludwig–Soret effect) is a phenomenon where a mass flow is induced by a gradient of temperature in a complex, at least binary, liquid [1–3]; it was observed for the first time almost 150 years ago [1]. The conventional hydrodynamic techniques using a thermodiffusion-flow cell [4, 5] were later enriched, for a faster determination of the Soret coefficient (S_T), by using optical methods such as small-angle Rayleigh scattering [6, 7], beam deflection [8–10], and forced Rayleigh scattering (FRS) [11–16].

While advances in thermodiffusion have focused primarily on dissolved polymers, studies on this effect in colloids, where the nanoparticle-diffusion coefficient is much smaller, are fairly recent developments [17–20]. The interferential FRS technique has enabled us first to measure the nanoparticle translational diffusion coefficient (D_M) in magnetic colloids (ferrofluids) [21, 22] and then to study the Soret effect in these materials [23, 24]. With this method,

the temperature variation is not only taken to generate a nanoparticle-concentration modulation in the colloid but is also used to calibrate it, which prevents us from performing difficult absolute photometry measurements; furthermore, the small sizes of the experiment, the cell size, and typical lengths in the heated part of the sample make the measurements rather insensitive to convection phenomena that could be generated by strong local density variations in the sample [15].

After a brief presentation of the ferrofluids and especially of the samples studied (section 2), a new FRS experimental set-up, simpler and cheaper than the conventional interferential one, is presented in section 3 [25]. In section 4 is given a two-dimensional theoretical analysis of the coupled evolutions of the temperature and the nanoparticle volume fraction in the sample using the new set-up. The index grating induced in the sample is probed by a cw He–Ne laser whose diffracted intensity is studied in section 5. Sections 6 and 7, are devoted, respectively, to theoretical and experimental studies of the decay of the high-order diffracted intensities after switching off the heating light. The accuracy of our

FRS method is analysed, allowing us to determine easily the translational nanoparticle-diffusion properties in different types of samples. In section 8 is given a method for determining the thermodiffusion coefficient (S_T) using the new set-up. Section 9 is devoted to experimental results obtained on S_T using this technique, with ferrofluids at various volume fractions, particle coatings, and dispersion liquids; some of them can be compared with the results found using the previous set-up. Appendices A and B are devoted to the numerical determinations of some data so as to validate the approximations used in sections 4, 5, 6, and 8.

2. Ferrofluids

Ferrofluids are colloidal suspensions of magnetic iron-oxide nanoparticles dispersed in a liquid medium. Interest in them arises from the fact that these liquids can be controlled by applying a magnetic field. The study of magnetic colloids started in 1965 through the pioneering patents of Papell and Rosensweig [26, 27]. Ferrofluids are incorporated into commercial and industrial processes; they find application in seals, bearings, dampers, etc, and more recently in biomedical applications [28, 29]. These systems are also at the origin of many theoretical papers in magnetism, optics, rheology, biophysics, and thermodynamics [30–32][3]. Ferrofluids are divided into two main groups, depending on the interparticle repulsion used to avoid their aggregation. According to the nature of the nanoparticle surface, the repulsion is either steric, when nanoparticles are coated with surfactants (surfaced ferrofluids), or electrostatic, when their surface bears charges (ionic ferrofluid). To obtain a ferrofluid, there are two basic steps: synthesis of the magnetic nanoparticles and then, by giving the nanoparticle surface suitable treatment, making a suspension in a carrier liquid.

The nanoparticle core of the ferrofluids studied here is made of maghemite (γ-Fe_2O_3). Nanoparticles are synthesized through a chemical process during which their size distribution is monitored in the nanometric range in order to obtain stable dispersions that would not settle under the action of gravity or of a magnetic field gradient. They are synthesized by a precipitation reaction occurring when mixing an aqueous mixture of $FeCl_2$ and $FeCl_3$ with ammonium hydroxide [33]. The so-obtained magnetite (Fe_3O_4) is then acidified, oxidized into maghemite, and dispersed into water, giving an ionic acidic ferrofluid (called IH). The nanoparticles are positively charged with nitrate (NO_3^-) counter-ions. This ferrofluid is then taken as a precursor for the samples studied. Adsorption of an ionic organic ligand (trisodium citrate) on these positive particles leads to an ionic ferrofluid (noted IC), stable in an aqueous medium (pH > 3); in this case, the nanoparticle surface charge is negative and neutralized by Na^+ counter-ions. To obtain a surfaced ferrofluid dispersed in cyclohexane, the nanoparticles are coated either with Beycostatne®, an industrial anionic surfactant (samples called SCB), or with oleic acid (sample called SCOA). The volume fraction of a ferrofluid is determined from chemical titration of iron [34]. Our nanoparticle-size data come from magnetization

[3] The bibliography about magnetic fluids is regularly summed up in the proceedings of the International Conference on Magnetic Fluids in a special issue of *J. Magn. Magn. Mater.*

measurements, and the distribution law for the nanoparticle magnetic core diameter (d) is assumed to be a lognormal one:

$$P(d) = \frac{1}{\sqrt{2\pi}\sigma d} \exp\left[-\frac{1}{2\sigma_m^2}\left(\ln\frac{d}{d_m}\right)^2\right].$$

For each sample, the mean magnetic diameter, d_m, and the distribution width, σ_m, are determined from magnetization measurements through a two-parameter fitting [35, 36]; the good fits found validate the assumption on the distribution law. Later, in this paper, we will use a volume-averaged magnetic diameter, d_m^V ($d_m^V = \langle d^3 \rangle^{1/3}$). In the case of a lognormal distribution law, we have $d_m^V = d_m \exp(1.5 \times \sigma_m^2)$. The constitutive characteristics of the samples studied here are given in table 1.

3. A new grid FRS set-up

In our previous FRS set-up, the spatial modulation of the heating light was obtained with a powerful pulsed frequency-doubled Nd : YAG laser beam split into two beams that interfere inside the sample [23]. In the new set-up shown in figure 1, the heating light source is a high pressure mercury arc lamp, and the spatial heating modulation is obtained by making, with a camera lens ($f = 50$ mm), the image of a periodic object in a 10–100 μm thick sample, perpendicular to the lens axis. In our experiments, objects are square-latticed metal grids with a wire diameter of about 0.4 mm and a period of about 1.4 mm. The image period, Λ_i, in the sample can be varied from 80 to 200 μm by moving the grid in the object space of the lens. The 'F number' is generally $f/2$.

The spatial modulation of temperature (T) induced in the sample yields a periodic modulation of the nanoparticle volume fraction (Φ) through the Soret effect. Both modulations induce diffracting gratings that are probed by a cw laser beam sent onto an area of the sample including the grid image; a He–Ne laser is chosen as its beam is weakly absorbed by magnetic colloids at $\lambda = 632$ nm. Therefore, as the partial derivatives ($\delta n'/\delta\Phi$ and $\delta n'/\delta T$) of the real part (n') of the refraction index of our samples at λ are much larger than those ($\delta n''/\delta\Phi$ and $\delta n''/\delta T$) of its small imaginary part (n''), these gratings are mainly index ones, which is convenient when interpreting diffraction data. Diffracted beams are detected, after filtering, with photomultiplier tubes having a highly linear response. In this study, problems associated with gravity such as convection, instabilities, or sedimentation (in the case of a nanoparticle Brownian energy lower than the gravitational potential energy gap between the top and bottom of the cell) are assumed not to occur. Anyway, to avoid these problems, experiments can be performed with a horizontal sample so that gravity plays the same role in any direction of the (Ox, Oy) plane (see inset in figure 1).

In our former FRS set-up, a pulsed pump laser (100 ps pulses gathered in 40 pulse trains (200 ns long) with a 10–1000 Hz repetition rate) was used so as to be able to determine the Soret coefficient with a linearized two-timescale model [23]. In the present set-up, the heating light source is a mercury arc lamp whose intensity is roughly proportional to the rectified power supply voltage, giving in Europe a 100 Hz time modulation. A model has then to be found for studying results obtained with the new set-up.

Table 1. Structure and properties of the ferrofluid samples studied here. All the samples share the same nanoparticle maghemite (γ-Fe$_2$O$_3$) core. In the surfaced samples SCB and SCOA, the nanoparticles are coated with Beycostatne® and oleic acid surfactant molecules, respectively, and are dispersed in cyclohexane (C$_6$H$_{12}$). In the ionic samples IC1 and IC2, the colloid is stabilized by citrate ions (negative surface charge) and Na$^+$ counter-ions (pH $\approx$ 7). In the ionic sample IH, the colloid is stabilized by H$^+$ ions (positive surface charge) with NO$_3^-$ counter-ions (pH $\approx$ 2). In all the ionic ferrofluids, the nanoparticles are dispersed in water. Their magnetic core diameters are observed to obey a lognormal distribution law with a mean magnetic core diameter of d_m, a distribution width of σ_m, and a volume average magnetic core diameter of d_m^V. The calibration factor, N^F, is the opposite of the ratio of the two partial derivatives $\partial n'/\partial \Phi$ and $\partial n'/\partial T$ of the ferrofluid refractive index; both are determined from measurements made with a total-refraction refractometer. The solvent viscosity, η, is found from [44]. In this table, the symbol $\approx$ before a number indicates a value estimated from nearby data.

| Surfaced ferrofluid samples							$\dfrac{\partial n'}{\partial \Phi}$	$10^4 \dfrac{\partial n'}{\partial T}$ (K^{-1})	N^F (K)	$10^3 \eta$ (Pa s) at 20°C
Solvent	Surfactant	Name	d_m (nm)/σ_m	d_m^V (nm)	Φ					
Cyclohexane	Beycostatne®	SCB1	7.5/0.37	9.2	2.27–6.8%		1.08	−5.6	1929	0.97
		SCB2	9.6/0.35	11.5	3.3–8.1%					
Cyclohexane	Oleic acid	SCOA	7/0.36	8.5	1.1–7.5%		$\approx$1.08	$\approx$ −5.6	$\approx$1929	0.97
Ionic ferrofluid samples										
Stabilization	Counter-ions	Name								
Citrate	Na+	IC1	9/0.35	10.8	3.3%		$\approx$1.32	$\approx$ −1.22	$\approx$10820	1.002
		IC2	8/0.30	9.15	1.3–6.5%		1.32	−1.22	10820	1.002
H$^+$	NO$_3^-$	IH	9/0.35	10.8	3.3%		$\approx$1.32	$\approx$ −1.22	$\approx$10820	1.002
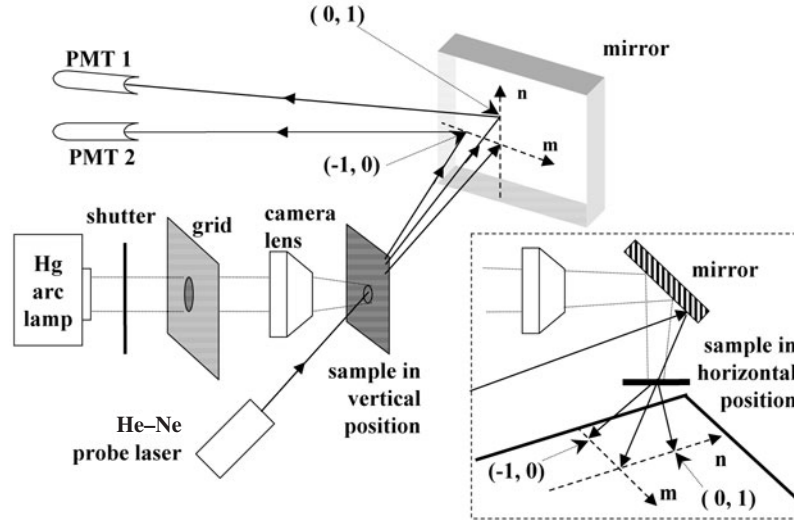
Figure 1. Experimental set-up. A camera lens makes in the sample the image of a grid lighted by a high pressure mercury arc lamp (100 Hz modulation in Europe). The index grating induced by both temperature and nanoparticle concentration modulations is probed by a cw He–Ne laser beam. Diffracted beams are detected by photomultiplier tubes (PMT) that have a highly linear response; only the $\{-10\}$ and $\{01\}$ beams are shown here. A set-up modification for studying horizontal samples is shown in the inset. A viewer (not shown here) is used to test that the grid image is in the sample plane.

4. Model for a two-dimensional two-timescale analysis

4.1. Two-dimensional temperature and concentration gratings

Our samples are ferrofluid layers of thickness l, located between two parallel glass plates that define the (Ox, Oy) plane. The nanoparticle volume fraction and the temperature in the sample can be written as

$$T(x, y, z, t) = T_0 + \delta T(x, y, z, t),$$
$$\Phi(x, y, z, t) = \Phi_0 + \delta \Phi(x, y, z, t), \tag{1}$$

where T_0 and Φ_0 are the initial homogeneous temperature and nanoparticle volume fraction, respectively, while $\delta T(x, y, z, t)$ and $\delta \Phi(x, y, z, t)$ are the variations of

temperature and volume fraction in the sample. In the absence of convection (small temperature and volume fraction variations, small typical lengths), these two thermodynamic variables obey the following continuity equations:

$$\rho c_p \frac{\partial T}{\partial t} = -\text{div} \, \vec{J}_{\text{th}} + \dot{Q} \tag{2}$$

and

$$\frac{\partial \Phi}{\partial t} = -\text{div} \, \vec{J}_M, \tag{3}$$

where $\vec{J}_{\text{th}}$ and $\vec{J}_M$ are the heat and nanoparticle volume fraction flows, respectively; ρ, c_p, and $\dot{Q}$ are the density of the colloid, its specific heat, and the heat input per unit time and unit volume, respectively. As experiments are performed at constant pressure and as the Dufour effect (heat flow induced by a nanoparticle volume fraction gradient) has been proved

to be negligible in our samples [23], the expression for $\vec{J}_{\text{th}}$ reduces to

$$\vec{J}_{\text{th}} = -\rho c_p D_{\text{th}} \vec{\nabla} T, \tag{4}$$

where D_{th} is the thermal diffusivity of the colloid, while $\vec{J}_M$ is written as

$$\vec{J}_M = -D_M(\vec{\nabla}\Phi + S_T \vec{\nabla}T), \tag{5}$$

where D_M is the nanoparticle diffusion coefficient and S_T is the Soret coefficient, so that the product $-S_T D_M \vec{\nabla}T$ is the thermodiffusion volume fraction flow [1–3]; we also define S_T^* by $S_T^* = S_T/\Phi$. These rather unusual definitions of S_T and S_T^* are taken from [23]. We recall that S_T is connected to some other parameters used in the literature, such as the thermal diffusion coefficient, $D_T = S_T^* D_M$, or the thermal diffusion factor, $\alpha_T = T S_T^*$ [37]. In any case, no *a priori* assumption has to be made about the variation of S_T, D_T, or α_T as functions of Φ, especially at rather high concentrations.

The components $J_{\text{th}\,z}$ and $J_{M\,z}$ along (Oz) of $\vec{J}_{\text{th}}$ and $\vec{J}_M$ are assumed to obey the following boundary conditions on the cell walls:

$$J_{\text{th}\,z}(x, y, 0, t) = -K_{\text{th}}^S[T(x, y, 0, t) - T_0],$$
$$J_{\text{th}\,z}(x, y, l, t) = K_{\text{th}}^S[T(x, y, l, t) - T_0], \tag{6}$$
$$J_{M\,z}(x, y, 0, t) = J_{M\,z}(x, y, l, t) = 0,$$

where K_{th}^S is an interface heat conductance (units of $\text{W m}^{-2}\,\text{K}^{-1}$) through each glass plate of the cell and where T_0 is also the temperature outside the sample (equation (1)). The first two conditions above express heat losses from the sample through the glass plates.

A three-dimensional solution of partial differential equations (2) and (3) with the above boundary conditions (equation (6)) can be found in [38]. However, for the sake of simplicity, the temperature and nanoparticle concentration variations along the Oz direction in the sample will not be taken into account in this paper. This is allowed because at least one of the two following conditions is fulfilled here: either $l < \Lambda_i$ or $\partial T/\partial z$ is negligible; the latter corresponds to weakly absorbing (diluted) samples for which l has to be chosen larger than Λ_i so as to obtain a measurable signal. For performing a two-dimensional approximation, we will use from now and without any danger of confusion the following functions, $T(x, y, t)$ and $\Phi(x, y, t)$, which are the averages of the temperature and the nanoparticle volume fraction over the cell thickness, l.

As shown in [23] and in appendix A, the amplitude of the temperature modulation and that of the nanoparticle volume fraction can be considered to be small when using both FRS techniques; D_M and S_T will therefore be assumed to be constant throughout the sample. From equations (3) and (5), the evolution of $\Phi(x, y, t)$ is then ruled by

$$\frac{\partial \Phi(x, y, t)}{\partial t} = D_M[\Delta\Phi(x, y, t) + S_T \Delta T(x, y, t)]. \tag{7}$$

Similarly, from equations (2), (4), and (6), $T(x, y, t)$ obeys the following partial derivative equation,

$$\frac{\partial T(x, y, t)}{\partial t} = D_{\text{th}}\Delta T(x, y, t) + \frac{\dot{Q}(x, y, t)}{\rho c_p}$$
$$-2\frac{K_{\text{th}}^{\prime S}}{l\rho c_p}[T(x, y, t) - T_0], \tag{8}$$

where $K_{\text{th}}^{\prime S}$ is the heat conductance of the interface modified for taking the present two-dimensional approximation into account and where $\dot{Q}(x, y, t)$ is now the heat input per unit time and unit volume of colloid due to the optical absorption averaged over the sample thickness, l. As $\dot{Q}$ is proportional to $I_p(x, y, t)$, the input heating beam intensity, it is written as

$$\dot{Q}(x, y, t) = \alpha I_p(x, y, t) \tag{9}$$

(for a monochromatic heating source $\alpha = (1 - \exp(-\varepsilon\Phi l))/l$, ε being the sample absorption coefficient at the heating wavelength per unit volume fraction).

The grids we use are periodic with, at least, a rectangular lattice where the (Ox) and (Oy) axes are symmetry ones. Assuming an infinite two-dimensional extension for the grid image, the heating-beam intensity, $I_p(x, y, t)$, in the sample can be Fourier expanded as

$$I_p(x, y, t) = I(t) \sum_{m=0}^{\infty} \sum_{n=0}^{\infty} c_{mn} \cos(mq_x x) \cos(nq_y y) \tag{10}$$

with

$$q_i = \frac{2\pi}{\Lambda_i} \qquad \text{with } i = x, y, \tag{11}$$

where Λ_i is the space period of the heating beam along the (Oi) direction inside the sample. Expression (10) would be different with asymmetric objects or another two-dimensional lattice (hexagonal for instance); such cases are not studied here. Similarly, the temperature modulation, $\delta T(x, y, t)$, can be Fourier expanded as

$$\delta T(x, y, t) = \sum_{m=0}^{\infty} \sum_{n=0}^{\infty} T_{mn}(t) \cos(mq_x x) \cos(nq_y y). \tag{12}$$

4.2. Two-timescale model

From equations (8), (9), (10), and (12), it is seen easily that the Fourier components, $T_{mn}(t)$, obey the following differential equation:

$$\frac{\text{d}T_{mn}}{\text{d}t} + \frac{T_{mn}}{\tau_{mn}^{\text{th}}} = W c_{mn} I(t) \tag{13}$$

with

$$W = \frac{\alpha}{\rho c_p} \tag{14}$$

and

$$(\tau_{mn}^{\text{th}})^{-1} = \frac{2K_{\text{th}}^{\prime S}}{l\rho c_p} + (m^2 q_x^2 + n^2 q_y^2)D_{\text{th}}; \tag{15}$$

it is worth noting that a non-zero value of $K_{\text{th}}^{\prime S}$ makes $(\tau_{00}^{\text{th}})^{-1}$ non-zero too. If the time period of the heating beam intensity, $I(t)$, is much larger than the thermal relaxation time, τ_{mn}^{th}, and if high order time Fourier components of $I(t)$ can be neglected, $T_{mn}(t)$ is proportional to $I(t)$ according to (equation (13)):

$$T_{mn}(t) = W \tau_{mn}^{\text{th}} c_{mn} I(t) \tag{16}$$

(valid even for m and $n = 0$). In this equation and in the following similar ones, no implicit summation is made on

m or on *n*. In the case of non-negligible high order time Fourier components of $I(t)$, a time shift between the minima of $T_{mn}(t)$ and $I(t)$ is seen; furthermore, the amplitude of the temperature modulation, $T_{mn}(t)$, is slightly less than that given in equation (16) [38]. Both phenomena will be neglected hereafter. In fact, in the previous works performed with the same sample thickness range, τ_{mn}^{th} has been shown to be less than 0.25 ms [23]. In the present experiments, the time period of the heating intensity (10 ms) is much larger than τ_{mn}^{th}, and equation (16) will be used in the following.

By assuming the same periodic two-dimensional infinite extension for the nanoparticle volume fraction, $\delta\Phi(x, y, t)$ can also be Fourier expanded as

$$\delta\Phi(x, y, t) = \sum_{m=0}^{\infty}\sum_{n=0}^{\infty} \Phi_{mn}(t)\cos(mq_x x)\cos(nq_y y). \quad (17)$$

From equations (7) and (16), $\Phi_{mn}(t)$ is seen to obey the following equations:

$$\Phi_{00} = 0$$

$$\frac{\mathrm{d}\Phi_{mn}(t)}{\mathrm{d}t} + \frac{\Phi_{mn}(t)}{\tau_{mn}^{M}} = -S_T\frac{T_{mn}(t)}{\tau_{mn}^{M}} \qquad \forall(m, n) \neq (0, 0)$$

$$(18)$$

with

$$(\tau_{mn}^{M})^{-1} = (m^2 q_x^2 + n^2 q_y^2)D_M; \quad (19)$$

Φ_{00} is zero because of the number conservation of nanoparticles. Solving equation (18) shows that, after a long enough elapsed time ($t \gg \tau_{mn}^{M}$), the component $\Phi_{mn}(t)$ of the volume fraction modulation tends to be periodic; its mean value, Φ_{mn}^{S}, is proportional to the time-averaged value, $\langle T_{mn}(t)\rangle$, of $T_{mn}(t)$ according to

$$\Phi_{mn}^{S} = -S_T\langle T_{mn}(t)\rangle \qquad \forall(m, n) \neq (0, 0). \quad (20)$$

Φ_{mn}^{S} can be also written as (equation (16))

$$\Phi_{mn}^{S} = -S_T W \tau_{mn}^{\text{th}} c_{mn} I_0 \qquad \forall(m, n) \neq (0, 0), \quad (21)$$

where I_0 is the time-averaged heating light intensity $I(t)$. A slight time-periodic modulation appears in $\Phi_{mn}(t)$, but it is easily proved to be undetectable because the period of the temperature modulation, $T_{mn}(t)$, i.e. that of the heating beam intensity ($\tau = 10$ ms), is much shorter than the nanoparticle concentration–relaxation time, τ_{mn}^{M} (of the order of 1 s). The nanoparticle volume fraction is quasi-steady for $t \gg \tau_{mn}^{M}$, and, for the sake of simplicity, we will study the Soret effect under this condition for t, following a reasoning similar to the one used for presenting the two-timescale model in [23]; $\Phi_{mn}(t)$ is then taken to be constant and equal to Φ_{mn}^{S}.

5. Probe laser beam diffracted intensities

The grating induced by both temperature and nanoparticle volume fraction modulations is probed by a cw He–Ne probe laser beam. Much information about the sample is found by analysing the intensity diffracted at several orders. In our experiment, the induced grating is found to work in the Raman and Nath regime (thin grating) according to Kogelnick *et al*'s

rule ($2\pi\lambda l/n'\Lambda_i^2 < 10$) [39] taking, at the worst, $\lambda = 632$ nm, $l = 100\,\mu$m (the grating being not thicker than the cell), $n' = 1.477$, and $\Lambda_i = 80\,\mu$m. The complex expression for the electromagnetic field, $\vec{E}^d(u, v)$, diffracted in the (u, v) Fourier plane direction is then written as

$$\vec{E}^d(u, v) = \vec{E}^* \exp\left(-\frac{2\pi l}{\lambda}n_0''\right)$$

$$\times \iint_{\Sigma} \exp\left(\mathrm{i}\frac{2\pi l}{\lambda}\delta n'\right)\exp(-\mathrm{i}(ux + vy))\,\mathrm{d}x\,\mathrm{d}y, \quad (22)$$

where $\vec{E}^*$ is the complex incident probe electromagnetic field, Σ is the area in the sample common to the grid image and the probe beam spot, and n_0'' is the imaginary part of the refractive index of the sample 'at rest'; the useless phase shift $((2\pi l/\lambda)n_0')$ is omitted and no $\delta n''$ contribution is taken into account [23]. As δT and $\delta\Phi$ are small, the n' modulation is simply

$$\delta n' = \frac{\partial n'}{\partial T}\delta T + \frac{\partial n'}{\partial\Phi}\delta\Phi. \quad (23)$$

Using the expressions for T_{mn} and Φ_{mn} in equations (16) and (21), $\vec{E}^d(u, v)$ is written as

$$\vec{E}^d(u, v) = \vec{E}^* \exp\left(-\frac{2\pi l}{\lambda}n_0''\right)$$

$$\times \iint_{\Sigma} \exp\left(\mathrm{i}\sum_{mn}\varphi_{mn}\cos(mq_x x)\cos(nq_y y)\right)$$

$$\times \exp(-\mathrm{i}(ux + vy))\,\mathrm{d}x\,\mathrm{d}y, \quad (24)$$

where the quantities φ_{mn} are defined as (equation (23))

$$\varphi_{mn} = \frac{2\pi l}{\lambda}\left(\frac{\partial n'}{\partial T}T_{mn} + \frac{\partial n'}{\partial\Phi}\Phi_{mn}\right). \quad (25)$$

By Taylor expanding the second exponential function in equation (24), $\vec{E}^d(u, v)$ is written as

$$\vec{E}^d(u, v) = \vec{E}^* \exp\left(-\frac{2\pi l}{\lambda}n_0''\right)$$

$$\times \iint_{\Sigma} \sum_{k=0}^{\infty}\frac{\mathrm{i}^k}{k!}\left(\sum_{mn}\varphi_{mn}\cos(mq_x x)\cos(nq_y y)\right)^k$$

$$\times \exp(-\mathrm{i}(ux + vy))\,\mathrm{d}x\,\mathrm{d}y. \quad (26)$$

To take the sharpness of the grid image into account, the expansions of *m* and *n* in equation (26) should be led up to a rather high order.

An optical coherent diffraction background is generally generated by unavoidable static defects in the volume lighted by the probe beam. By taking it into account together with the incoherent background contribution to the diffracted signal, the intensity, I^d, measured in the (u, v) direction is expressed as

$$I^d(u, v) = \tfrac{1}{2}\Sigma\varepsilon_0 c\|\vec{E}^d(u, v) + \vec{E}^c(u, v)\|^2 + I^{\text{nc}}(u, v), \quad (27)$$

where I^{nc} is the non-coherent background intensity in the (u, v) direction, while $\vec{E}^c(u, v)$ is the coherent background EM field. It can be factorized as

$$\vec{E}^c(u, v) = \vec{E}^*[g^r(u, v) + \mathrm{i}g^i(u, v)], \quad (28)$$

g^r and g^i being the real and imaginary parts of the ratio $E^c(u, v)/E^*$; in both the above complex equations, the phase difference between $\vec{E}^d$ and $\vec{E}^c$ is clearly expressed. Using also

equation (28), algebraic expressions can be found for $I^d(u, v)$ as a function of φ_{mn}, g^r, and g^i. However they are too long to be presented in a table, but they can be established easily with the help of 'Mathematica' or 'Maple' software. The upper limits for the k, m, and n expansions will be studied from experimental results in the following section. The usual Bessel's function expansion in equation (24) would have led to very complicated expressions except for the case when m and $n \leqslant 1$. The $\{ij\}$ notation for a two-dimensional diffraction order is defined by $i = u/q_x$ and $j = v/q_y$.

6. Diffracted signal decay

If we wait a time longer than the thermal relaxation time after switching off the heating light (at $t = 0$ in this section), the temperature modulation becomes negligible and no Soret process occurs any more. The concentration grating remains then the only one, and its slow decay can be studied easily from diffraction measurements.

6.1. General study

The decay of the volume fraction component, $\Phi_{mn}(t)$, is expressed as (equations (18) and (21))

$$\Phi_{mn}(t) = -S_T c_{mn} W \tau_{mn}^{\text{th}} I_0 \exp(-D_M (m^2 q_x^2 + n^2 q_y^2) t). \quad (29)$$

Setting T_{mn} to zero in equation (25), $\varphi_{mn}(t)$ is then written as

$$\varphi_{00}(t) = 0,$$
$$\varphi_{mn}(t) = \varphi_{mn}^0 \exp(-D_M (m^2 q_x^2 + n^2 q_y^2) t) \ \forall (m, n) \neq (0, 0), \quad (30)$$

where

$$\varphi_{mn}^0 = -\frac{2\pi l}{\lambda} \frac{\partial n'}{\partial \Phi} S_T W I_0 c_{mn} \tau_{mn}^{\text{th}}. \quad (31)$$

The diffracted intensity decay is still given by equations (26) and (27), where φ_{mn} is made explicit by equation (30).

6.2. Case of a square-latticed grid

For a square-latticed grid, the c_{mn} coefficients can be factorized as

$$c_{mn} = c_{nm} = c_m(r) c_n(r), \quad (32)$$

where

$$c_0(r) = r,$$
$$c_{n \neq 0}(r) = (-1)^n \frac{2}{n\pi} \sin(nr\pi) \quad (33)$$

and where $r = (\Lambda - d_w)/\Lambda$, d_w being the grid wire diameter and Λ the period of the grid square-lattice. The grid image in the sample maintains the ratio r, but the above formula for $n \neq 0$ is only valid for the grid image, i.e. the heating intensity, if the camera lens is of good enough quality. Taking $q_x = q_y = q$, equation (30) reduces to

$$\varphi_{mn}(t) = \varphi_{mn}^0 \exp\left(-(m^2 + n^2) \frac{t}{\tau^M}\right), \quad (34)$$

where

$$\frac{1}{\tau^M} = q^2 D_M. \quad (35)$$

The diffracted intensity functions, $I_{ij}^d(t)$, can be expanded as the following series of decreasing exponential functions,

$$I_{ij}^d(t) = \sum_{p=0}^{\infty} I_{ijp}^d \exp\left(-p \frac{t}{\tau^M}\right) + I_{ij}^{\text{nc}}, \quad (36)$$

where I_{ij}^{nc} is the non-coherent background intensity measured in the direction defined by the $\{ij\}$ order of diffraction. Algebraic expressions for I_{ijp}^d or, more precisely, for I_{ijp}^d/I^*, where I^* is the incident probe intensity ($I^* = \frac{1}{2} \sum \varepsilon_0 c \|\vec{E}^*\|^2$), obtained from equations (26), (27), and (28) with the help of Mathematica, are summed up for $\{ij\} = \{10\}$, $\{11\}$, and $\{20\}$ in table 2, for $p \leqslant 8$ (equation (36)) and with the following limitations on equation (26): $k \leqslant 2$, $m \leqslant 3$, and $n \leqslant 3$ ($I_{ij}^d(t) = I_{ji}^d(t)$ by the symmetry property).

7. Experimental results from decay studies

In this section, the decay of the nanoparticle volume fraction grating is studied by checking the decays of intensities diffracted at various orders, for three purposes: (i) testing the validity and the accuracy of the calculations developed above, (ii) evaluating the coherent background contributions, and (iii) determining τ^M, then D_M (equation (35)), and finally the hydrodynamic diameter, d_H, using Stokes–Einstein's equation ($3\pi \eta d_H D_M = k_B T$). As the heating duration is much larger than τ^M, the value we obtain for d_H is that of a volume averaged hydrodynamic diameter [40].

The three experimental intensity curves, $I_{10}^d(t)$, $I_{11}^d(t)$, and $I_{20}^d(t)$, shown in figure 2, are found from experiments performed with the SCB2—3.3% sample. They should obey equation (36), the expressions for I_{ijp}^d being given in appendix B, which is tested by a best-fit procedure where the ten following parameters τ^M, g_{kl}^r, g_{kl}^i, and C_{ij} (proportionality factors defined in appendix B) are determined. The other quantities, φ_{mn}^0 and I_{ij}^{nc}, in equation (36), are previously, respectively, evaluated from input power measurements (appendix A) and incoherent background measurements (by switching off the probe laser beam). As τ^M is common to the three expressions for $I_{ij}^d(t)$, the best-fit procedure has to be carried out with the three curves simultaneously.

7.1. Model validity and approximations in signal analyzing

The fitting procedure gives back best-fit curves very close to the experimental ones (figure 2), which proves the three diffraction signals ($\{10\}$, $\{11\}$, and $\{02\}$ directions) share the same time constant, τ^M, as intended in the section 6 description. Mathematically, each one of the three diffracted signals carries enough information for determining the same transport properties and the coherent background contribution at the same time. If the diffracted signals can be measured with enough accuracy, it is enough to work only on one order of diffraction, and in this case, the first-order signal ($\{01\}$ or $\{10\}$) is the easiest one to study because (i) it is the most intense and (ii) equation (B.1) is simpler than equations (B.2) and (B.3) (appendix B). This observation validates former works where only signals diffracted at the first-order (even with one-dimensional experiments) were studied. Another technique, the 'homodyne/heterodyne'

Table 2. Algebraic I_{ijp}^d/I^* expressions for $(i, j) = (1, 0)$, $(1,1)$, and $(2,0)$ according to equation (36) obtained with the help of Mathematica from equations (25), (26), (27), and (28) with the following restrictions: $k \leqslant 2$; m, $n \leqslant 3$; and $p \leqslant 6$.

| p	$\dfrac{I_{10p}^d}{I^*}$	$\dfrac{I_{11p}^d}{I^*}$	$\dfrac{I_{20p}^d}{I^*}$
0	$(g_{10}^r)^2 + (g_{10}^i)^2$	$(g_{11}^r)^2 + (g_{11}^i)^2$	$(g_{20}^r)^2 + (g_{20}^i)^2$
1	$2g_{10}^i\varphi_{10}^0$	0	0
2	$(\varphi_{10}^0)^2$	$-g_{11}^r(\varphi_{10}^0)^2 + 2g_{11}^i\varphi_{11}^0$	$-\frac{1}{2}g_{20}^r(\varphi_{10}^0)^2$
3	$-g_{10}^r\varphi_{10}^0\varphi_{11}^0 - \frac{3}{4}g_{10}^i(\varphi_{10}^0)^3$	0	0
4	$-\frac{3}{4}(\varphi_{10}^0)^4$	$(\varphi_{11}^0)^2 + \frac{1}{4}(\varphi_{10}^0)^4 - \frac{3}{4}g_{11}^i(\varphi_{10}^0)^2\varphi_{11}^0$	$\frac{1}{16}(\varphi_{10}^0)^4 - \frac{1}{4}g_{20}^r(\varphi_{11}^0)^2 + \frac{1}{2}g_{20}^i(4\varphi_{20}^0 - (\varphi_{10}^0)^2\varphi_{11}^0)$
5	$-g_{10}^r\varphi_{10}^0\varphi_{20}^0 - \frac{3}{8}g_{10}^i\varphi_{10}^0(\varphi_{11}^0)^2$	0	0
6	$-\frac{1}{8}(\varphi_{10}^0)^2(\varphi_{11}^0)^2 + \frac{9}{64}(\varphi_{10}^0)^6$	$-\frac{3}{4}(\varphi_{10}^0)^2(\varphi_{11}^0)^2 - g_{11}^r(\varphi_{10}^0\varphi_{21}^0 + \varphi_{11}^0\varphi_{20}^0)$ $- g_{11}^i(\frac{3}{32}(\varphi_{11}^0)^3 + (\varphi_{10}^0)^2\varphi_{20}^0)$	$\frac{1}{16}(\varphi_{10}^0)^2(\varphi_{11}^0)^2 - g_{20}^r\varphi_{10}^0\varphi_{21}^0 - g_{20}^i(\varphi_{10}^0)^2\varphi_{20}^0$
7		0	0
8			$(\varphi_{20}^0)^2 + \frac{1}{16}(\varphi_{10}^0)^4(\varphi_{11}^0)^2 + \frac{1}{64}(\varphi_{11}^0)^4 - \frac{1}{2}(\varphi_{10}^0)^2\varphi_{11}^0\varphi_{20}^0$ $+ \frac{1}{4}(\varphi_{10}^0)^3\varphi_{21}^0 - g_{20}^i(\frac{3}{8}(\varphi_{11}^0)^2\varphi_{20}^0 + \frac{3}{4}\varphi_{10}^0\varphi_{11}^0\varphi_{21}^0)$
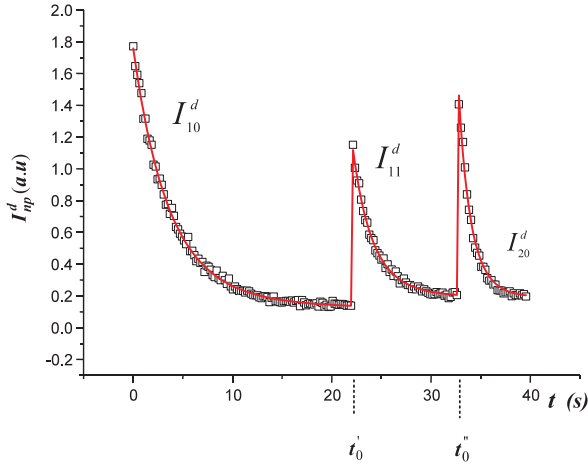
Figure 2. Decay of the nanoparticle concentration grating. The experimental diffracted intensity curves (arbitrary units), I_{10}^d, I_{11}^d, and I_{20}^d, as functions of time. For a clearer presentation, simultaneous curves are abscissa shifted. The experiment is performed with a BNE-surfaced ferrofluid sample dispersed in cyclohexane (sample SCB2—3.3%). A best-fit procedure applied to equations (B.1), (B.2), and (B.3) gives τ^M, g_{ij}^r, g_{ij}^i, and C_{ij} parameters that give back well fitting curves. For determination of D_M, and S_T, the linearized version of the square-grid model is then validated by the weak values found for φ_{mn}^0 (appendix B), g_{ij}^r, and g_{ij}^i. The relaxation time found for τ^M (6.5 s) is consistent, through Stokes–Einstein's equation, with previous results on the nanoparticle size [42, 43].

one [41], gives more precise results on the coherent background with a one-dimensional interferential set-up; a similar 'homodyne/heterodyne' technique could be developed later with a two-dimensional set-up!

Less general conclusions can be drawn from the best-fit values found with the SCB2 sample.

(i) Among the terms where a grating contribution appears, the dominant one is given by $p = 2(i^2 + j^2)$, which is not surprising as this term is built from the lowest power terms and, as in the case of weak heating (δT small), $\varphi_{01} \leqslant 1$ and φ_{mn} is a decreasing function of $(m^2 + n^2)$ (appendix B). Therefore, increasing the upper limits for the k, m, n,

and p expansions would not improve the determination accuracy.

(ii) The coherent background contribution can be neglected in the I_{ij}^d expression of equations (B.1), (B.2), and (B.3) in appendix B when the g_{ij}^r and g_{ij}^i dependent coefficients of the time exponential terms are much smaller than the coefficients independent of g_{ij}^r and g_{ij}^i of the first exponential term due to the concentration grating only. We can see that for the {10} diffracted signal, this condition is verified if $5.68 \times 10^{-5}g_{10}^r$ and $2.24 \times 10^{-2}g_{10}^i$ are smaller than 1.26×10^{-4}, i.e. if g_{10}^r and g_{10}^i are less than 1 and 10^{-2}, respectively. But for the {11} and {20} diffracted signal, the background contribution can be neglected if g_{ij}^r and g_{ij}^i are less than 10^{-1} and 10^{-3}, respectively. In our experiment, the best-fit values found for g_{ij}^r and g_{ij}^i are about 10^{-3} to 5×10^{-3}. The coherent background contribution can then be neglected in the {10} diffracted signal, but on the contrary, it cannot be neglected when studying the {11} and {20} diffracted signals.

Gathering the above partial conclusions for the determination of D_M leads us to study only the {10} signal, to consider only its $p = 2$ term, and to neglect any coherent background. This observation made with one sample is however quite general, and the coherent background can be neglected in the {01} diffraction signal, with all the samples exhibiting low enough diffuse scattering, i.e. with all the samples we studied. These conclusions also validate previous FRS works [11–16, 21, 22].

For further determination of S_T, we will use the above conclusion about the determination of D_M: we will study only the {10} signal, consider only its $p = 2$ term, and neglect any coherent background. Will these approximations still hold when studying highly concentrated colloids where strong absorption or large optical scattering is seen?

7.2. Results on translational nanoparticle diffusion

The above best-fit procedure gives a relaxation time of 6.5 s and therefore a nanoparticle diffusion coefficient, D_M, of 26.5×10^{-12} m² s⁻¹ (equation (35)) with $\Lambda_i = 82.5\,\mu$m.

Table 3. The nanoparticle diffusion coefficients, D_M, are measured using both interferential and grid FRS setups, either according to the method given in section 6 with the SCB2 surfaced ferrofluid or according to the method given in [21] with the other samples. The hydrodynamic nanoparticle diameter, d_H, is found from D_M through Stokes–Einstein's equation using results from two-dimensional experiments when available and interferential ones when not. The effective coating thickness, e_{ef}, is defined by $(d_H - d_m^V)/2$. S_T^* is the reduced Soret coefficient ($S_T^* = S_T/\Phi$). Values for D_M and S_T^* given here are averages from many experiments. The Soret mobility, μ_S, which characterizes the Soret velocity response to a temperature gradient, is found through equation (47). In this table, the symbol $\approx$ before a number indicates a value estimated from nearby data.

Surfaced ferrofluids	$10^{12} \, D_M$ (m^2 s^{-1})		d_H (nm)	e_{ef} (nm)	$S_T^* = S_T/\Phi$ (K^{-1})		$10^{-9} \, \mu_S$ (kg^{-1} s)	
	Pulsed laser heating	Hg arc lamp heating			Pulsed laser heating	Hg arc lamp heating	Pulsed laser heating	Hg arc lamp heating
SCB1	30.6	29.6	15.0	2.9	0.131	0.104	290	223
SCB2	31.3	26.5	16.7	2.6	0.155	0.164	352	315
SCOA	$\approx$31.5	31.5	14.1	2.8	0.041	0.043	93.4	98.2
Ionic ferrofluids								
IC1	27	$\approx$27	15.9	2.5	-0.123	-0.0839	-241	-164
IC2	49.3	$\approx$49.3	8.73	-0.2	-0.0142	-0.0138	-50.7	-49.3
IH	36	$\approx$36	11.9	0.5	-0.076	-0.11	-198	-287

With a cyclohexane viscosity, η, of 0.97×10^{-3} Pa s at 20°C [44], it gives a hydrodynamic diameter, d_H, of 16.7 nm, which is in good agreement with the mean volume average magnetic diameter of about 11.5 nm found from magnetization measurements (table 1) if we take the thicknesses of the nonmagnetic layer (0.8–1.0 nm) and the surfactant molecule layer ($\sim$2 nm) into account [42, 43].

The values (averages from many measurements) we obtain for D_M and d_H with different ionic and surfaced samples are summed up in table 3. Noting that the hydrodynamic diameter is a volume averaged diameter, the d_H values can be connected tentatively with those of d_m^V shown in table 1 by defining an effective coating thickness, e_{ef}, as $(d_H - d_m^V)/2$ (see table 3). Experiments are performed with both, interferential and grid, FRS setups; it is seen clearly that both setups provide consistent results. With both setups, diffraction measurements are performed only at the first-order of diffraction, as allowed by the above conclusion (section 7.1), with the only exception of the above study performed with the sample SCB2 using the grid set-up. Our different samples exhibit quite similar diffusion characteristics, with the noticeable exception of the sample IC2. With surfaced ferrofluids, the effective coating thickness is remarkably constant, whatever the surfactant, and consistent with the above data in [42, 43]. The ionic samples have various effective coating thicknesses and in particular a 'small' negative value is found with sample IC2. This last value is not inconsistent if it is remembered that e_{ef} is the difference between two data that do not come strictly from the same distribution laws (magnetic core and hydrodynamic), but anyway with this sample, the average citrate layer must be very thin (see further comments on S_T).

8. Determination of the Soret coefficient

For determination of the Soret coefficient according to the two-timescale model presented in section 4.2, it is necessary to be able to distinguish in the diffraction signal the part of the signal due to the concentration grating alone from that given by the superposition of both thermal and nanoparticle concentration modulations. It is made possible by using a mercury arc lamp,

whose intensity is rather well approximated as

$$I(t) = \frac{\pi}{2} I_0 |\sin(\omega t)|, \tag{37}$$

where I_0 is again the mean value of $I(t)$; note $I(t)$ is modulated at the frequency of the rectified power supply voltage ($F = 2(\omega/2\pi)$). As the thermal relaxation time, τ_{mn}^{th} (0.2–2 ms) is much shorter than the heating time period ($\tau = 1/F = 10$ ms), the sample temperature follows the time variation of the heating light intensity according to (see equation (16))

$$T_{mn} = \frac{\pi}{2} c_{mn} W \tau_{mn}^{th} I_0 |\sin(\omega t)|, \tag{38}$$

whereas as the relaxation time, τ_{mn}^M, of the nanoparticle grating is larger than τ ($\tau_{mn}^M \approx 0.5$–5 s), the volume fraction modulation components tend to the steady state value, Φ_{mn}^S (see equation (21)). Similarly, under this nanoparticle-concentration steady state condition, φ_{mn} can be expressed as (equation (25))

$$\varphi_{mn} = \left(\frac{2\pi l}{\lambda} c_{mn} W \tau_{mn}^{th} I_0\right) \left(\frac{\pi}{2} \frac{\partial n'}{\partial T} |\sin(\omega t)| - \frac{\partial n'}{\partial \Phi} S_T\right)$$
$$\forall (m, n) \neq (0, 0). \tag{39}$$

As with our samples, we have $\partial n'/\partial T < 0$ and $\partial n'/\partial \Phi > 0$, the two elementary refractive index gratings due to the temperature and nanoparticle concentration modulations are in phase if the nanoparticles move towards colder regions; conversely, if nanoparticles move towards warmer regions, the two gratings have opposite phases.

As shown in section 7, $k > 1$ terms and high order φ_{mn} components give negligible contributions to $I_{10}^d(t)$, at least with our set-up and our samples; the coherent background contribution has been shown to be negligible too. Therefore, $I_{10}^d(t)$ is expressed accurately enough by taking only $k = 1$ and φ_{10} (or φ_{01}) in equation (26) and setting $\vec{E}^c(u, v) = \vec{0}$ in equation (27). In the following lines, the incoherent background is omitted, but it is easy to take into account when it is measurable.

At the quasi-steady state of the nanoparticle volume fraction, the first-order diffracted intensity of the probe beam,
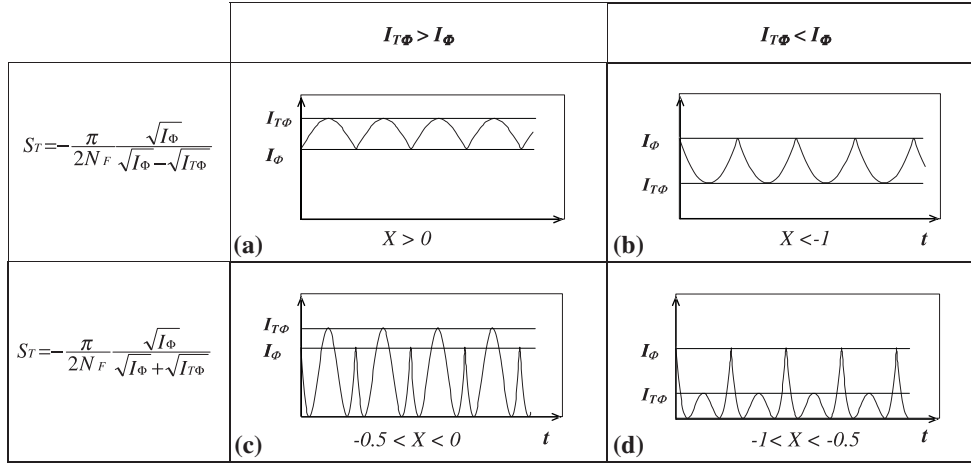
Figure 3. Theoretical first-order diffracted intensity, $I_{10}^d(t)$, curves can take four different shapes according to the value of the parameter X (equation (40)). The shape of each experimental $I_{10}^d(t)$ curve is compared with the four theoretical ones so as to choose in what domain X lies (the sharp extrema in the experimental curves are sometimes not so easy to distinguish from the smooth ones). For each shape, a formula is given to determine S_T from the experimental data, N_F, I_Φ, and $I_{T\Phi}$ (equation (46)).

$I_{10}^d(t)$, can then be approximated as

$$I_{10}^d(t) \propto I^*(\varphi_{10})^2 = I^* \left(\frac{\pi^2 l}{\lambda} c_{10} W \tau_{10}^{\text{th}} I_0 \frac{\partial n'}{\partial T} \right)^2$$
$$\times (|\sin(\omega t)| + X)^2, \tag{40}$$

where X is a dimensionless quantity defined as

$$X = \frac{2}{\pi} N^F S_T, \tag{41}$$

N^F being a temperature-dimensioned calibration factor defined as follows:

$$N^F = -\frac{\partial n'/\partial \Phi}{\partial n'/\partial T}. \tag{42}$$

Denoting by $I_{T\Phi}$ the first-order diffracted intensity when both gratings take place simultaneously, the thermal grating being at its maximum, $I_{T\Phi}$ is expressed as

$$I_{T\Phi} = I_{10}^d|_{|\sin(\omega t)|=1} \propto (1 + X)^2, \tag{43}$$

whereas when the nanoparticle volume fraction grating is the only one in the sample, the first-order diffracted intensity, denoted I_Φ, is simply given by

$$I_\Phi = I_{10}^d|_{|\sin(\omega t)|=0} \propto X^2. \tag{44}$$

Equations (43) and (44) give the following relation between X and the ratio $I_\Phi/I_{T\Phi}$:

$$X^2 \left(\frac{I_{T\Phi}}{I_\Phi - 1} \right) - 2X - 1 = 0. \tag{45}$$

The value of S_T is then determined by choosing the right expression between the two solutions, S_T^+ and S_T^-, expressed as (equation (41))

$$S_T^\pm = -\frac{\pi}{2N^F} \frac{1}{1 \pm \sqrt{I_{T\Phi}/I_\Phi}}. \tag{46}$$

The choice is made by comparing the shape of the experimental $I_{10}^d(t)$ curve with the four possible different shapes that $I_{10}^d(t)$

may have; all four are plotted in figure 3, and the corresponding expression for determining S_T is given for each of them. The linear approximation used above leads to an algebraic evaluation of S_T that depends only on the ratio $I_{T\Phi}/I_\Phi$ and therefore where no absolute experimental determination of light intensities is needed.

9. Soret effect with surfacted and ionic colloids

Figures 4(a) and (b) show typical intensity curves at a short timescale for $I_{10}^d(t)$ during the quasi-steady state of the nanoparticle volume fraction, with the samples SCB1—6.8% and IC1, respectively. It is seen clearly that the temperature contribution exhibits the heating light periodicity. With the sample SCB1, the experimental $I_{10}^d(t)$ curve (figure 4(a)) has the same shape as the one given in figure 3(a), thus proving S_T is positive. On the contrary, the Soret coefficient of the sample IC1 is found to be negative because the experimental $I_{10}^d(t)$ curve (figure 4(b)) has the figure 3(b) shape. However, in these curves, surfacted colloids give, in proportion, a higher thermal contribution than the ionic ones, and this phenomenon was observed with almost all the other samples we studied (here and in [23, 24]). This effect is easily understood by checking equation (46) with the definition of N^F (equation (42)) and noting that, with our samples, $|S_T|$ is of the same order of magnitude for both types of ferrofluids. As the value of $\partial n'/\partial \Phi$ is mostly ruled by the nature of the nanoparticle core, it is of the same order of magnitude with our different samples (table 1). On the contrary, $\partial n'/\partial T$ is mainly given by the nature of the solvent; $|\partial n'/\partial T|$ is about five times smaller with water (the dispersion liquid of the ionic samples) than with organic solvents in which the surfacted ferrofluids studied were dispersed (see table 1).

In figures 5(a) and (b) are given experimental plots of S_T as a function of Φ with the samples SCOA (surfacted) and IC2 (ionic), respectively. Note again that $S_T > 0$ with the surfacted sample, whereas $S_T < 0$ with the ionic one. It is also seen that S_T is proportional to Φ, at least for $\Phi < 10\%$, which confirms the results obtained previously with other ferrofluid samples [23].

(a) $I_{10}^d (a.u.)$

$t\ (10^{-2}\ s)$

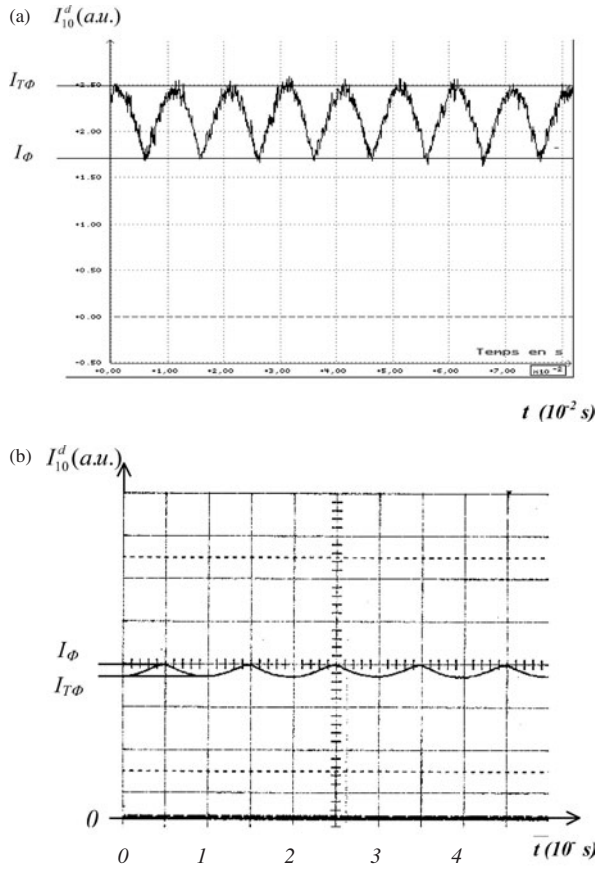(b) $I_{10}^d (a.u.)$

$t\ (10^6\ s)$

Figure 4. (*a*) Typical short timescale response curve of the first-order diffracted intensity, $I_{10}^d(t)$, during the particle volume fraction quasi-steady state; the experiment is performed with a BNE-surfaced ferrofluid dispersed in cyclohexane (sample SCB1—6.8%). The experimental curve has the same shape as the theoretical one shown in figure 3(*a*) ($S_T > 0$). The refraction index gratings due to both temperature and concentration modulations are in phase, proving nanoparticles move towards the coldest regions. (*b*) Typical short timescale response curve of the first-order diffracted intensity, $I_{10}^d(t)$, during the particle volume fraction quasi-steady state; the experiment is performed with a citrated ionic ferrofluid (sample IC1). The experimental curve has the same shape as the theoretical one shown in figure 3(*b*) ($S_T < 0$). The refraction index gratings due to both temperature and concentration modulations have opposite phases, proving nanoparticles move towards the warmest regions.

The volume fraction flow due to the Soret effect alone $(-D_M S_T \vec{\nabla} T)$ can also be expressed as the product $\Phi \vec{v}_S$, where $\vec{v}_S$ is the nanoparticle mean drift velocity due to the Soret effect alone. The Soret mobility, μ_S, defined by the expression $\vec{v}_S = -\mu_S \vec{\nabla}(k_B T)$ [23], can be then determined from the following relation,

$$\mu_S = D_M \frac{S_T(\Phi)}{k_B \Phi}, \qquad (47)$$

where Boltzmann's constant, k_B, is used to keep to μ_S the usual mobility dimension. As S_T is observed to be proportional to the nanoparticle volume fraction, Φ, in any type (surfaced or ionic) of ferrofluid and as D_M does not vary very much within the same concentration range (see equation (5) in [22]), μ_S is seen not to depend on Φ for $\Phi < 10\%$. The Soret
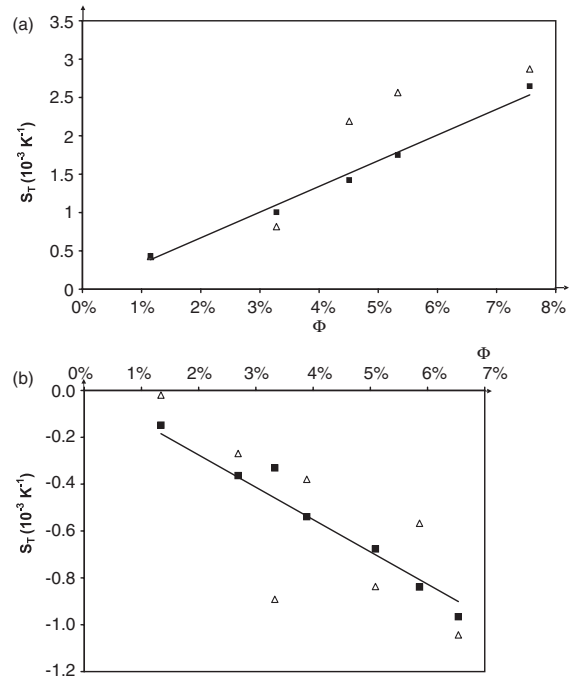
(a)

(b)

Figure 5. (*a*) Plot of the Soret coefficient, S_T, as a function of Φ with the surfaced sample SCOA. The experiments are performed with the interferential FRS set-up ($\triangle$) and the new grid FRS set-up ($\blacksquare$). Consistent results are provided by the two setups. A linear regression made only with the new FRS set-up results gives $S_T^* = S_T/\Phi = 0.033\ \mathrm{K}^{-1}$. (*b*) Plot of the Soret coefficient, S_T, as a function of Φ with the ionic sample IC2. The experiments are performed with the FRS laser set-up ($\triangle$) and the new FRS grid set-up ($\blacksquare$). Consistent results are provided by the two setups. A linear regression made only with the new FRS set-up results gives $S_T^* = S_T/\Phi = -0.014\ \mathrm{K}^{-1}$.

effect is then proved to be a nanoparticle property, at least for $\Phi < 10\%$. The algebraic values of S_T^* ($S_T^* = S_T/\Phi$) and μ_S we obtained with different ionic and surfaced samples are summed up in table 3. Experiments performed with both (interferential and grid) FRS setups provide consistent results. No variation with the incident intensity, I_0, has been observed in S_T when studying a citrated sample, which is consistent with the linearized master equations of the Soret effect.

An improvement in the precision of the knowledge about the origin of the Soret effect can be attained. Almost all the ferrofluids we studied (here and in [23, 24]) were made of nanoparticles that share the same magnetic maghemite core, but these samples differ in the nanoparticle coating and the dispersion liquid. The origin of the Soret effect is then to be found in the whole formed by the (surfactant or ionic) nanoparticle coating and the region of the dispersion liquid in the vicinity of each nanoparticle [45–47]; the thickness of this 'surrounding whole' could be estimated tentatively by the effective thickness, e_{ef}, defined in section 7.2. The two SCB samples were not synthesized and studied in the same years, but they clearly exhibit, rather close properties. On the contrary, the samples SCB and SCOA, which differ in the nature of the surfactant molecules (table 1), give quite different positive values for S_T^* although their e_{ef} values are very near. The two citrated ionic samples, IC1 and IC2, give quite different values for S_T^* and e_{ef} (table 3); however, it is worth noting that

the sample that gives a small value of $|S_T^*|$ is the one where e_{ef} has been seen to be very small too. These remarks should be followed by deeper investigations.

10. Conclusion

The new FRS set-up presented in this paper for determination of the nanoparticle diffusion coefficient and the Soret coefficient, is cheaper and smaller than our previous interferential one using a pulsed heating laser. With this new set-up, the image period, Λ_i, in the sample can be varied by moving the grid in the object space of the lens, taking grids with other periods or varying the focal length of the camera lens; the diffracting geometry can even be modified by making images of objects that are not grids. Furthermore, the heating light spectrum can be modified easily by using optical filters or by changing, at a low cost, the nature of the arc lamp. The two-dimensional nanoparticle volume fraction grating induced by the Soret effect opens a way for observing two-dimensional movements of nanoparticles. It could be used for studying nanoparticle transport along two directions submitted to different physical conditions simultaneously (such as those induced by gravity or an external magnetic field).

This simple experimental set-up can be used easily to study the mass transport properties of other colloids that have transport characteristics near those of ferrofluids. Other materials such as binary mixtures that exhibit a larger mass diffusion coefficient ($D_M \approx 10^{-10} \, \text{m}^2 \, \text{s}^{-1}$) could be studied with such a set-up as their mass diffusion coefficient would be still much smaller than their thermal diffusion coefficient ($D_{\text{th}} \approx 10^{-8}$–$10^{-7} \, \text{m}^2 \, \text{s}^{-1}$ [14, 16]), but it would be needed to change the period, Λ_i, of the image in the sample or to increase the frequency of the heating light (when possible) so as to maintain the validity of the present model ($\tau^M > \tau > \tau^{\text{th}}$).

In this paper, the first-order approximation used in section 7 for determination of Soret properties is justified by theoretical and experimental studies (section 6) on intensities diffracted at high orders during the vanishing process of the nanoparticle volume fraction grating. Therefore the numerical calculations given in appendix B, which need previous knowledge of S_T and absolute determination of I_0, are useless from now. In this case, only relative light intensity measurements are needed for determinations of S_T and D_M because they are used in ratios such as that seen in equation (46). Nevertheless, the above complete theoretical study could be useful for analyzing results from experiments exhibiting larger coherent backgrounds or non-negligible intensities diffracted at high orders.

The nanoparticle diffusion properties and the experimental values of the Soret coefficient, S_T^*, in ferrofluid samples obtained with this set-up are of the same order of magnitude as those obtained previously from interferential FRS experiments. As was observed before, the Soret coefficient of the citrated and acidic ionic samples is found to be negative, in contrast to that measured with our surfaced ones (positive sign of S_T). It confirms the fact that the Soret coefficient of a ferrofluid is dependent strongly on the nature of the carrier liquid, the nature of the stabilization, and the surface charge of the nanoparticle; by studying other types of ferrofluids, this dependence has been shown to be

rather complicated [24]. The non-dependence on Φ we observe for μ_S seems to exclude any nanoparticle–nanoparticle interaction; although it is quite normal at low nanoparticle concentrations, this observation is more surprising at high Φ because, for instance, the mean distance between two near nanoparticles is only about twice their diameter at $\Phi = 10\%$. To our knowledge, no theoretical model published so far sheds light on the Soret effect mechanism in magnetic colloids completely [45,46], but a general framework has been proposed recently [47].

Acknowledgments

Appendix A. Small δT and $\delta \Phi$ assumption validity

The linearized model presented above is valid if D_M and S_T can be considered as constant all over the sample, i.e. if δT and $\delta \Phi$ are small enough (equation (1)). Taking the following data on the surfaced sample SCB2, $2K_{\text{th}}'^S/l\rho c_p = 4000 \, \text{s}^{-1}$, $D_{\text{th}} = 1.0 \times 10^{-7} \, \text{m}^2 \, \text{s}^{-1}$, and $\rho c_p = 1.5 \times 10^6 \, \text{J m}^{-3} \, \text{K}^{-1}$ from [23], with $S_T/\Phi = 0.164 \, \text{K}^{-1}$ (table 3), we finally find by noting $\bar{T}_{ij} = \langle T_{ij}(t) \rangle$ (equation (16))

$$\begin{aligned}
&\bar{T}_{00} = 0.0498 \, \text{K} && \bar{T}_{20} = -0.0137 \, \text{K} \\
&\bar{T}_{10} = -0.0303 \, \text{K} && \bar{T}_{21} = 0.008\,74 \, \text{K} \\
&\bar{T}_{11} = 0.0187 \, \text{K} && \bar{T}_{22} = 0.004\,35 \, \text{K} \\
&\qquad \bar{T}_{30} = -0.002\,78 \, \text{K} \\
&\qquad \bar{T}_{31} = 0.001\,82 \, \text{K} \\
&\qquad \bar{T}_{32} = 0.000\,97 \, \text{K} \\
&\qquad \bar{T}_{33} = 0.000\,22 \, \text{K}
\end{aligned}$$

and (equation (20))

$$\begin{aligned}
&\Phi_{00}^S = 0 && \Phi_{20}^S = 4.72 \times 10^{-5} \\
&\Phi_{10}^S = 1.04 \times 10^{-4} && \Phi_{21}^S = -3.01 \times 10^{-5} \\
&\Phi_{11}^S = -6.46 \times 10^{-5} && \Phi_{22}^S = -1.5 \times 10^{-5} \\
&\qquad \Phi_{30}^S = 9.59 \times 10^{-6} \\
&\qquad \Phi_{31}^S = -6.29 \times 10^{-6} \\
&\qquad \Phi_{32}^S = -3.33 \times 10^{-6} \\
&\qquad \Phi_{33}^S = -7.89 \times 10^{-7}
\end{aligned}$$

under the following experimental conditions: $\Phi = 3.3\%$ and $l = 10 \, \mu\text{m}$, $\Lambda_i = 82.5 \, \mu\text{m}$, $r = 5/7$, and $I_0 = 7077 \, \text{W m}^{-2}$. The first two conditions lead to a value for α of $52\,700 \, \text{m}^{-1}$ and a rate of power absorption by the sample of 53%. The maximum values for δT and $\delta \Phi/\Phi$ are then found to be $0.0026 \, \text{K}$ and 0.5%, respectively, which is small enough to validate the linear approximations used in the model (equations (17), (38), (21), and (12)).

Appendix B. Expansions for the intensity, I_{ijp}^d, diffracted by a decaying concentration grating

To find explicit numerical expressions for I_{ijp}^d (equation (36)), the coefficients φ_{mn}^0 have to be determined previously from

equations (14), (15), and (31). Taking the same experimental conditions as in appendix A, we find

$$\varphi_{10}^0 = 1.12 \times 10^{-2} \qquad \varphi_{20}^0 = 5.06 \times 10^{-3}$$
$$\varphi_{11}^0 = -0.693 \times 10^{-2} \qquad \varphi_{21}^0 = -3.23 \times 10^{-3}$$
$$\varphi_{22}^0 = -1.61 \times 10^{-3}$$
$$\varphi_{30}^0 = 10.3 \times 10^{-4}$$
$$\varphi_{31}^0 = -6.75 \times 10^{-4}$$
$$\varphi_{32}^0 = -3.57 \times 10^{-4}$$
$$\varphi_{33}^0 = -0.85 \times 10^{-4}$$

As assumed in the model, φ_{mn}^0 is much less than 1 and clearly a decreasing function of $(m^2 + n^2)$. Using the data of table 2, it gives the following expressions for the three first diffracted intensities I_{ij}^d:

$$I_{10}^d(t) = I_{10}^{\text{nc}} + C_{10} \left[(g_{10}^r)^2 + (g_{10}^i)^2 + 2.24 \times 10^{-2} g_{10}^i \right.$$
$$\times \exp\left(-\frac{t}{\tau^M}\right) + 1.26 \times 10^{-4} \exp\left(-\frac{2t}{\tau^M}\right)$$
$$\left. + 5.68 \times 10^{-5} g_{10}^r \exp\left(-\frac{3t}{\tau^M}\right) \right], \qquad (B.1)$$

$$I_{11}^d(t) = I_{11}^{\text{nc}} + C_{11} \left[(g_{11}^r)^2 + (g_{11}^i)^2 - (1.26 \times 10^{-4} g_{11}^r \right.$$
$$+ 1.39 \times 10^{-2} g_{11}^i) \exp\left(-\frac{2t}{\tau^M}\right) + 4.8 \times 10^{-5}$$
$$\left. \times \exp\left(-\frac{4t}{\tau^M}\right) + 7.13 \times 10^{-5} g_{11}^r \exp\left(-\frac{6t}{\tau^M}\right) \right], \quad (B.2)$$

$$I_{20}^d(t) = I_{20}^{\text{nc}} + C_{20} \left[(g_{20}^r)^2 + (g_{20}^i)^2 - 6.28 \times 10^{-5} g_{20}^r \right.$$
$$\times \exp\left(-\frac{2t}{\tau^M}\right) + (-1.20 \times 10^{-5} g_{20}^r + 1.01 \times 10^{-2} g_{20}^i)$$
$$\times \exp\left(-\frac{4t}{\tau^M}\right) + 3.6 \times 10^{-5} g_{20}^r \exp\left(-\frac{6t}{\tau^M}\right)$$
$$\left. + 2.56 \times 10^{-5} \exp\left(-\frac{8t}{\tau^M}\right) \right], \qquad (B.3)$$

where C_{ij} are proportionality coefficients related to photometry measurements. The three expansions above are limited to a level p defined by the lowest term that does not depend on g_{ij}^r or g_{ij}^i (other high p terms are retained when having the same order of magnitude).

References

[1] Ludwig C 1856 *S-B. Akad. Wiss. Wien* **20** 539
[2] Soret C 1879 *Arch. Sci. Phys. Nat. Genève* [3] **2** 48
[3] de Groot S R 1945 *L'effet Soret* (Amsterdam: NV Noord-Hollandsche Uitgevers Maatschappij)
[4] Thomaes G 1956 *J. Chim. Phys.* **53** 407
[5] Ecenarro O, Madariaga J A, Navarro J, Santamaria C M, Carrion J A and Saviron J M 1990 *J. Phys.: Condens. Matter* **2** 2289
[6] Li W B, Segré P N, Gammon R W and Sengers J V 1994 *Physica* A **204** 399
[7] Segré P N, Gammon R W and Sengers J V 1993 *Phys. Rev.* E **47** 1026
[8] Giglio M and Vendramini A 1975 *Phys. Rev. Lett.* **34** 561
[9] Kolodner P, Williams H and Moe C 1988 *J. Chem. Phys.* **88** 6512
[10] Jean-Jean B, Freysz E, Ponton A, Ducasse A and Pouligny B 1989 *Phys. Rev.* A **39** 5268
[11] Allain C and Lallemand P 1977 *C. R. Acad. Sci. Paris* B **285** 187
[12] Thyagarajan K and Lallemand P 1978 *Opt. Commun.* **26** 54
[13] Bloisi F and Vicari L 1987 *Appl. Phys.* B **44** 103
[14] Köhler W 1993 *J. Chem. Phys.* **98** 660
[15] Freysz E, Laffon E, Delville J P and Ducasse A 1994 *Phys. Rev.* E **49** 2141
[16] Köhler W and Müller B 1995 *J. Chem. Phys.* **103** 4367
[17] Jeon S J, Schimpf M E and Nyborg A 1997 *Anal. Chem.* **69** 3442
[18] Tabiryan N V and Luo W 1998 *Phys. Rev.* E **57** 4431
[19] Schaertl W and Roos C 1999 *Phys. Rev.* E **60** 2020
[20] Spill R, Köhler W, Lindenblatt G and Schaertl W 2000 *Phys. Rev.* E **62** 8361
[21] Bacri J-C, Cebers A, Bourdon A, Demouchy G, Heegaard B M and Perzynski R 1995 *Phys. Rev. Lett.* **74** 5032
[22] Bacri J-C, Cebers A, Bourdon A, Demouchy G, Heegaard B M, Katshevsky B and Perzynski R 1995 *Phys. Rev.* E **52** 3936
[23] Lenglet J, Bourdon A, Bacri J C and Demouchy G 2002 *Phys. Rev.* E **65** 31408
[24] Alves S, Demouchy G, Bee A, Talbot D, Bourdon A and Figueiredo Neto A M 2003 *Phil. Mag.* **83** 2059–66
[25] Mezulis A 1999 *PhD Thesis* Université Paris 7-Denis Diderot, Paris
[26] Papell S S 1965 *US Patent* no 3 215572
[27] Rosensweig R E 1985 *Ferrohydronamics* (Cambridge: Cambridge University Press)
[28] 1994 *Magnetic Fluids and Applications—Handbook* ed B Berkovsky and M Khartov (New York: Begell House)
[29] Halbreich A, Roger J, Pons J N, Geldwerth D, Da Silva M F, Roudier M and Bacri J-C 1998 *Biochimie* **80** 379–90
[30] Fabre P, Casagrande C, Veyssié M, Cabuil V and Massart R 1990 *Phys. Rev. Lett.* **64** 539
[31] Bacri J-C and Figueiredo Neto A M 1994 *Phys. Rev.* E **50** 3860
[32] Bibette J 1993 *J. Magn. Magn. Mater.* **122** 37
[33] Massart R 1981 *IEEE Trans. Magn.* **17** 1247
[34] Charlot G 1966 *Les méthodes de la Chimie analytique, analyse quantitative minérale* (Paris: Masson et Cie) pp 737
[35] Bacri J-C, Perzynski R, Salin D, Cabuil V and Massart R 1986 *J. Magn. Magn. Mater.* **62** 36–46
[36] Massart R, Dubois E, Cabuil V and Hasmonay E 1995 *J. Magn. Magn. Mater.* **149** 1
[37] de Groot S R and Mazur P 1962 *Non-Equilibrium Thermodynamics* (Amsterdam: North-Holland) p 278
[38] Blums E, Mezulis A and Bourdon A 1999 *Proc. 3rd Baltic Heat-Transfer Conf.* ed B J Grochal *et al* (Gdansk: Institute of Fluid-Flow Machinery Publishers) *Progress Eng. Heat Transfer*
[39] Kogelnik H 1969 *Bell Syst. Tech. J.* **48** 2909
[40] Rossmanith P and Köhler W 1996 *Macromolecules* **29** 3203
[41] Köhler W and Rossmanith P 1995 *J. Phys. Chem.* **99** 5838
[42] Blums E Ya, Cebers A O and Maiorov M M 1997 *Magnetic Fluids* (Berlin, New York: Walter de Gruyter)
[43] Fertman V 1988 *Magnitnye Zhidkosti* Vyshejshaya Shkola, Minsk
[44] 1995 *Handbook of Chemistry and Physics* 75th edn, ed D R Lide (Boca Raton: CRC Press) pp 6–244
[45] Morozov K I 1999 *J. Exp. Theor. Phys.* **88** 944
[46] Morozov K I 2002 *Thermal Nonequilibrium Phenomena in Fluid Mixtutures* (*Lecture Notes in Phys.* vol 584) ed W Köhler and S Wiegand (Berlin: Springer) pp 38–60
[47] Bringuier E and Bourdon A 2003 *Phys. Rev.* E **67** 011404